Available online at www.sciencedirect.com

ScienceDirect

journal homepage: www.elsevier.com/locate/he

Modeling photovoltaic-electrochemical water splitting devices for the production of hydrogen under real working conditions

*Alexa Grimm, Alix Sainte-Marie, Gert Jan Kramer, Matteo Gazzani**

Utrecht University, Princetonlaan 8a, 3584 CB Utrecht, the Netherlands

HIGHLIGHTS

- Modeling photoelectrochemical water splitting devices.
- Framework based on steady-state equivalent circuit.
- Comparing performance under ideal and real irradiation and varying tilt angle.
- The most performing device varies depending on the irradiation.
- A higher ideal STH efficiency does not necessarily mean a better performance.

GRAPHICAL ABSTRACT

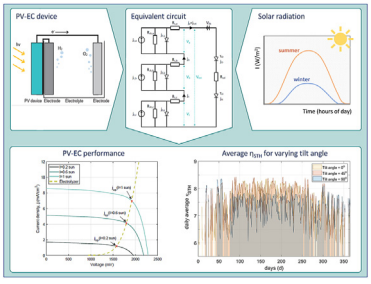

ARTICLE INFO

Article history:
Received 24 November 2021
Received in revised form
27 January 2022
Accepted 28 January 2022
Available online 20 February 2022

Keywords:
Solar water-splitting
Hydrogen
Photoelectrochemical cell
PV-EC

ABSTRACT

Photoelectrochemical splitting of water is potentially a sustainable and affordable solution to produce hydrogen from sun light. Given the infancy stage of technology development, it is important to compare the different experimental concepts and identify the most promising routes. The performance of photoelectrochemical devices is typically measured and reported under ideal irradiation conditions, i.e. 1 sun. However, real-life operating conditions are very different, and are varying in time according to daily and seasonal cycles.

In this work, we present an equivalent circuit model for computing the steady state performance of photoelectrochemical cells. The model allows for a computationally efficient, yet precise prediction of the system performance and a comparison of different devices working in real operating conditions. To this end, five different photoelectrochemical devices are modeled using experimental results from literature. The calculated performance shows good agreement with experimental data of the different devices. Furthermore, the model is extended to include the effect of illumination and tilt angle on the hydrogen production efficiency. The resulting model is used to compare the devices for different locations with high and low average illumination and different tilt angles. The results show that including real illumination data has a considerable impact on the efficiency of the PV-EC device. The yearly average solar-to-hydrogen efficiency is

* *Corresponding author.*
E-mail address: m.gazzani@uu.nl (M. Gazzani).

https://doi.org/10.1016/j.ijhydene.2022.01.223

significantly lower than the ideal one. Moreover, it is dependent on the tilt angle, whose optimal value for European-like latitude is around 40°. Notably, we also show that the most performing device through the whole year might not necessarily be the one with highest sun-to-hydrogen efficiency for one-sun illumination.

Nomenclature

General

EC	electrochemical
HER	hydrogen-evolving reaction
OER	oxygen-evolving reaction
PC	photocatalytic
PE	photoelectrodes
PEC	photoelectrochemical
PV	photovoltaic
PV-E	photovoltaic + electrolyzer
SLJ	solid-liquid junction
STH	solar-to-hydrogen

Parameters

$\hat{j}_L$	nominal photogenerated current density, mA/cm^2
$\hat{P}_{sun}$	ideal illumination, sun
$\Delta\overline{G^0}_{H_2}$	Gibbs free energy, kJ/g
η_F	Faradaic efficiency
η_{STH}	solar to hydrogen efficiency
τ_H	Tafel slope of HER, mV/dec
τ_O	Tafel slope of HER, mV/dec
a	specific area, m^2/t$_{H2}$
E°	thermodynamic potential
e^{year}_{H2}	energy stored in hydrogen molecules in a square meter of PV-EC over the year, kJ/m^2
j	current density, mA/cm^2
j_0	saturation (dark) current density, mA/cm^2
j^0_H	exchange current density at HER, mA/cm^2
j_L	photogenerated current density, mA/cm^2
j^0_O	exchange current density at OER, mA/cm^2
k_B	Boltzmann constant, J/K
m^{year}_{H2}	hydrogen produced over the year per square meter, t$_{H2}$/m^2
n_i	ideality factor
n_j	number of junctions
n_s	number of solar cells connected in series
P_{sun}	real illumination, mW/cm
q	elementary charge, C
R_s	series resistance, Ω/cm^2
R_{sh}	shunt resistance, Ω/cm^2
R_{sol}	electrolyte solution resistance, $\Omega.cm^2$
T	temperature, K
V	voltage, mV
V_{th}	thermal voltage 25.9 mV at T = 300K

Introduction

Hydrogen will play a pivotal role in the transition towards a climate neutral society. Its end use in a net-zero CO_2 world will be widespread and diverse: from fuel for ground and air transportation, to feedstock for the chemical industry, via energy carrier for seasonal storage in power generation [1]. However, today 95% of hydrogen is produced by hydrocarbon steam reforming, a process emitting around 830 million tonnes of CO_2 per year [1]. Clearly, this is not sustainable. Ultimately, within this century and probably by 2050, the vast majority of H_2 will need to be produced starting from renewable energy, with the remaining coming from fossil sources with carbon capture and storage. One such way is via electrochemical splitting of H_2O using renewables-based electricity. In this context, solar photoelectrochemical water splitting is a sustainable pathway, that uses the most abundant renewable energy source available, the sun, to produce hydrogen. The water splitting reaction is an endothermic reaction at ambient condition with a net free Gibbs energy ΔG^0 of 237.2 kJ/mol, which corresponds to a potential (E°) of 1.23 V. The two redox half-reactions occurring at the electrodes are (i) water oxidation at the anode (Eq. (1)), or oxygen evolving reaction (OER), and (ii) water reduction at the cathode (Eq. (2)), or hydrogen evolving reaction (HER):

$$2H_2O \rightleftharpoons O_2 + 4H^+ + 4e^- \quad (1)$$

$$4H^+ + 4e^- \rightleftharpoons 2H_2 \quad (2)$$

Solar water splitting, or photolysis of water, is not a new concept; the first experimental demonstration of the splitting of water into hydrogen and oxygen by electrocatalysis was reported by Fujishima and Honda in 1972, who used a rutile titanium dioxide (TiO_2) photoanode and a Pt counter electrode [2]. Since the conduction band of rutile is not negative enough to split H_2O, an applied voltage bias was applied to the TiO_2 working electrode. Although TiO_2 material is stable in aqueous electrolytes, the performance is low due to its large band gab (3.2 eV), which limits the utilization of the solar spectrum to the UV portion.

Since then, an increasing number of experimental concepts has been assembled and tested, improving the technology significantly (e.g. Refs. [3–5]). As expected, most studies focused on developing more performant materials for the different components of the device, or on designing optimal reactor configurations to achieve higher solar-to-hydrogen (STH) efficiencies [6]. Notably, solar water splitting systems

involve five main ingredients, namely a photoabsorber that converts photons into electron-hole pairs, a catalyst of the oxygen-evolving reaction, a catalyst of the hydrogen-evolving reaction, an electrolyte allowing the protons transportation from one electrode to the other, and, for most reactor designs, a membrane to separate the products.

Depending on the materials used and the design of the system, different types of solar water splitting devices can be identified. In literature, various taxonomies for the different cells can be found, e.g. in Refs. [7–9], where detailed reviews of the different solar fuel generators are presented. In Fig. 1, a simplified overview of the different types and sub-types of solar water splitting devices is given. Three main approaches can be identified: photocatalytic (PC), photoelectrochemical (PEC), and photovoltaic + electrolyzer (PV-E). The presented overview should not be seen as a strict categorization, since there exist also devices that could be attributed to more than one of these categories. Rather, with the presented classification we focus on technological and modeling aspects.

A PC device consists of suspended particles of photocatalyst dispersed in a medium. It is the simplest system, since there is only one light absorber, however, the simplicity is paid with low STH efficiencies, which are in the range of 1% [10,11]. On the other side of the spectrum, combining PV cells with an electrolyzer is a modular approach using two systems: PV panels producing independent power are connected to an electrolyzer (or several electrolyzers). Due to significant advances in solid state photovoltaics, PV-E systems are today the most efficient way to carry out solar water splitting, yielding STH efficiencies as high as 30% [12]. PEC devices lie in the middle, as the integrated version of a PV-E system, where the light absorber is immersed in the electrolyte. Because semiconductors are very sensitive to corrosion, the light absorber has to be protected from the electrolyte, affecting the overall STH efficiency of the system. Typical STH efficiencies of PEC devices range from 1 to 20% [13].

The architecture of a PEC device is mainly based on the type of junction used to separate the electron-hole pair. Band bending, resulting from a local imbalance in charge neutrality, is the phenomenon responsible for the charge separation and transfer in a PEC device. Band bending occurs at a junction between a semiconductor and another material and depends on the type of junction. Two junctions can be found in a PEC device: a buried PV junction and a solid-liquid junction (SLJ). In a buried PV junction (also called Schottky-junction), the interface between a metal and a semiconductor is responsible for band bending. A buried junction works together with at least one p-n junction, located at the interface between two layers of a semiconductor, one doped positively (p) and the other doped negatively (n). Together, the buried junction and the p-n junction(s) drive efficiently the electrons and holes apart. On the other hand, a solid-liquid junction is located at the interface between a semiconductor and a liquid solution. The effect is the same as in a buried PV junction since it permits the charge separation and transfer between the photoabsorber and the electrolyte. However, a single SLJ is not sufficient to drive the water splitting reaction without any additional bias, thus, a tandem architecture is necessary [14]. PEC devices can be further divided in sub-categories as shown in Fig. 1: (i) a PEC device with one or more buried PV junctions and two or more p-n junctions (also known as PV-EC device), (ii) a PEC device with one buried PV junction coupled with one solid liquid junction (PV-PEC), and (iii) a dual photoelectrode with two SLJ (Dual-PE).

PV-EC technology benefits from the well-established knowledge of water electrolysis on the one hand, and photovoltaics on the other hand, and can easily achieve STH efficiencies of more than 10% [13]. Several PV-EC devices have been built using various PV technologies such as crystalline silicon [15], thin film (e.g. amorphous silicon (a-Si) [16], copper indium gallium selenide (CIGS) solar cells [17]), and multijunction solar cells [18]. Recently, Cheng and coworkers have demonstrated a record STH efficiency of 19.3% with a monolithic PV-EC device consisting of a GaInP/GaInAs multijunction [19].

On the other hand, PV-PEC devices are hybrid systems combining both a buried PV junction with p-n junction(s) and a SLJ. In this configuration, the PV cell provides the voltage bias necessary for the photoelectrode to drive the water splitting reaction. Such devices are generally built to study and improve the photoelectrode [20].

In a dual-PE device, two different absorbers are in contact with the electrolyte solution, resulting in two SLJs, one at each photoelectrode. This design benefits from cheaper materials but exhibits lower STH efficiencies, around 1% [13]. Multiple studies focus on dual photoelectrodes devices to improve the efficiency of the system. To date, the highest STH efficiency was achieved by using a $BiVO_4$ photoanode with a CIGS photocathode and reached 3.7% [21].

While dual photoelectrode technology is in its infancy, PV-EC and PV-PEC systems are more mature [14]. This work focuses on PV-EC because of the maturity and relative simplicity of the technology but also due to the better experimental data availability.

While there exist studies providing a detailed overview of the state-of-the-art of solar water splitting devices [22–25], there are no works that focus on modeling and comparing different PV-EC devices under ideal and real light conditions. One reason is that research efforts currently focus mainly on finding innovative materials and architectures to improve the overall performance of the system. As a result, it is difficult to identify the preferred direction of development among the many materials and devices presented in literature. Moreover, the effect of illumination on the hydrogen production efficiency has been largely overlooked in past works, with the exception of Turan et al., who investigated the scale up PV-EC devices [6]. With this work, we aim at contributing to close these gaps by (i) providing a consistent modelling framework of different PV-EC devices using the equivalent electric circuit approach, and by (ii) predicting and comparing the yearly hydrogen production rate under real-world illumination and varying tilt angles. This work is organized as follows: Section Modeling PV-EC systems with equivalent electric circuit describes the modeling methodology and resulting performance of five different PV-EC devices using the equivalent electric circuit approach, first for ideal conditions, second for varying illumination and tilt angle. This is followed by a yearly comparison of the different devices (Section Comparison of PV-EC cells under varying working conditions). Finally, we discuss the resulting findings.

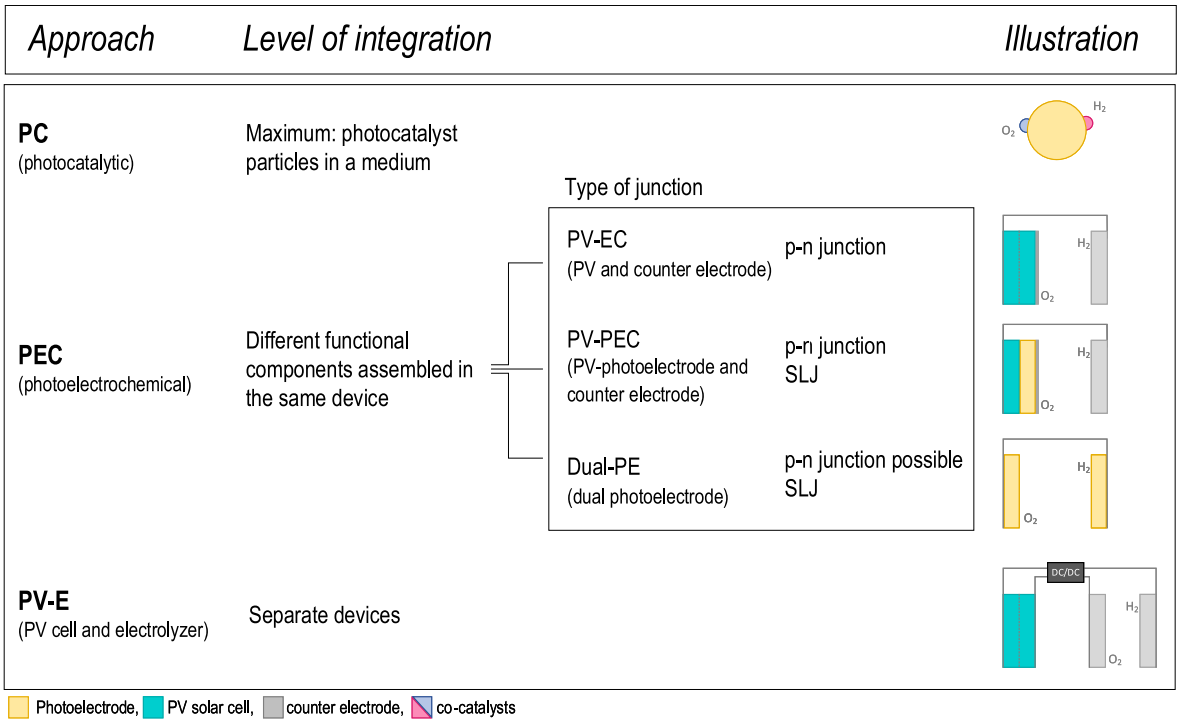

Fig. 1 – Different types of solar water splitting devices. PEC cells are divided into photovoltaic-electrochemical (PV-EC) devices, photovoltaic-PEC (PV-PEC) devices and devices with two photoelectrodes (Dual-PE). For each configuration a typical example is illustrated.

Modeling PV-EC systems with equivalent electric circuit

In the following, we first present and validate a model for simulating PV-EC using the equivalent electric circuit approach. For the validation we use experimental data from literature. Then, we extend the model to include varying illumination conditions, which allows for computing yearly performance including weather data of different geographical locations. The obtained model is finally used to compare different PV-EC devices at varying (i) location, and (ii) tilt angle.

PV-EC model for ideal sun conditions

Our modeling framework builds upon and extends the work of Winkler et al., who modeled an integrated PV-EC device using steady-state equivalent circuits [26]. The approach of equivalent circuit is relatively simple, yet accurate in describing the behaviour of a PV-EC system. To this end, the device can be divided into two main components: a photoabsorber part, consisting of the different light absorbers and later referred as the 'solar cell', and an electrolyzer part, which includes the two electrodes (the catalysts and/or a metal) and the electrolyte solution. A simplified scheme of a PV-EC device is shown in Fig. 2. We note that the solar cell and the catalysts can be either directly in contact or wired, but since the losses due to the wires are negligible, we will no further make a differentiation between the two. To model the thermodynamic performance of the system, we need the j-V curves of PV and EC sides as shown in Fig. 2. The cell operating point is identified by the intersection of the two j-V curves, which depend on the specific materials and architecture.

The overall electric equivalent circuit of a generic multi-junction PV-EC system is shown in Fig. 3. Each p-n junction in the photoabsorber is represented by a one diode model consisting of a source of current j_L, a diode defined by saturation current density j_0, a series resistance R_s and a shunt resistance R_{sh}. The source of current j_L represents the photogenerated current, while the diode represents the recombination current induced by the recombination losses of electrons and holes. Both series and shunt resistance are parasitic elements to represent ohmic losses in the PV device. The equivalent steady-state circuit of the electrolyzer part of the system is shown on the right in Fig. 3. In this model, the thermodynamic potential is depicted by a voltage source, while the resistance R_{sol} represents the voltage drop caused by the electrolyte solution.

The current density of the photoabsorber can be calculated by taking the photogenerated current j_L and subtracting all recombination currents according to the equivalent curcuit model [26]. The resulting equation is:

$$j = \frac{1}{n_s}\left[j_L - j_0 exp\left(\frac{\frac{V}{n_j} + jR_s}{n_i V_{th}}\right) - \frac{\frac{V}{n_j} + jR_s}{R_{sh}}\right] \quad (3)$$

where:

- V_{th} is the thermal voltage, i.e. the voltage induced in the p-n junction by the ambient temperature and is calculated based on the Boltzmann constant k_B, the temperature T and the elementary charge q: $V_{th} = \frac{k_B T}{q}$. At room temperature V_{th} is equal to approximately 26 mV.
- n_j is the number of junctions (e.g. 3 for a triple junction as shown in Fig. 3).
- n_s is the number of solar cells connected in series, respectively.

The voltage calculated with Equation (3) is the voltage output of one single photoabsorber junction. If a solar cell consists of multiple junctions or if several single junction solar cells are connected in series, the total voltage output is given by the sum of the voltage of each junction [27]:

$$V = \sum_i^{n_j} V_i \tag{4}$$

which simplifies to $V = n_j V_i$ if the n_j junctions are identical.

Since the solar cells and the electrolyzer are connected in series, the current is the same in all the components. In case that n_s identical solar cells are connected in series, the photoabsorber area is then multiplied by the number of cells and the current density of the total system is:

$$j_{tot} = \frac{j}{n_s} \tag{5}$$

In order for the electrolyzer to split H_2O, the solar cell(s) must produce a voltage accounting for the thermodynamic potential E° of the water splitting reactions (OER and HER) (1.23 V), and the voltage loss at the cathode and the anode and ohmic losses of the solution. Therefore, the electrolyzer voltage can be written as:

$$V_{electrolyzer} = E^\circ + V_{cathode}^{loss} + V_{anode}^{loss} + R_{sol} j \tag{6}$$

The voltage loss at the cathode and anode can be calculated using the Tafel law, which connects the rate of the electrochemical reactions of the electrode to the overpotential:

$$V_{cathode}^{loss} + V_{anode}^{loss} = \tau_H log_{10}\frac{j}{j_H^0} + \tau_O log_{10}\frac{j}{j_O^0} \tag{7}$$

where the terms τ_O and τ_H are the Tafel slopes, j_O^0 and j_H^0 are the exchange current densities and where the subscripts O and H refer to the OER and HER respectively. The overall equation for the electrolyzer is therefore written as:

$$V_{electrolyzer} = E^\circ + \tau_H log_{10}\frac{j}{j_H^0} + \tau_O log_{10}\frac{j}{j_O^0} + R_{sol} j \tag{8}$$

The system operating point is found evaluating the photoabsorber and electrolyzer voltage (or current) which is obtained in practice by directly coupling or wiring together the two:

$$\sum_i V_{PV,i} = V_{electrolyzer} \tag{9}$$

The resulting equivalent circuit model of the PV-EC system (Equations (3)–(9)) requires different empirical parameter as input: j_L, j_0, R_s, R_{sh}, n_i for the solar cell and τ_H, τ_O, j_H^0, j_O^0, R_{sol} for the electrolyzer part. These can be obtained by fitting the model equations with available experimental points for a specific device, which requires the expression of the equations in the form $V = f(V)$ or $j = f^{-1}(V)$. This can be tackled by using the Lambert function (more details can be found in the

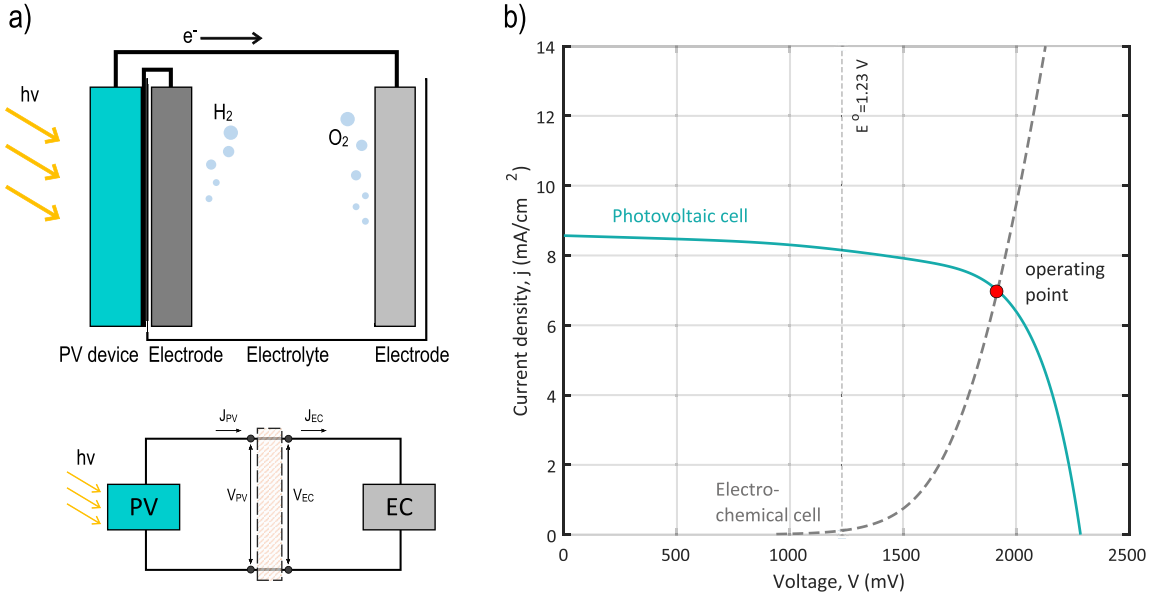

Fig. 2 – (a) A simplified setup of an exemplary PV-EC device, and of a PV device which provides power to an electrochemical cell (adapted from Refs. [13,26]). (b) Simplified j-V characteristics of a PV-EC device, the operating point is indicated by a red dot. (For interpretation of the references to color in this figure legend, the reader is referred to the Web version of this article.)

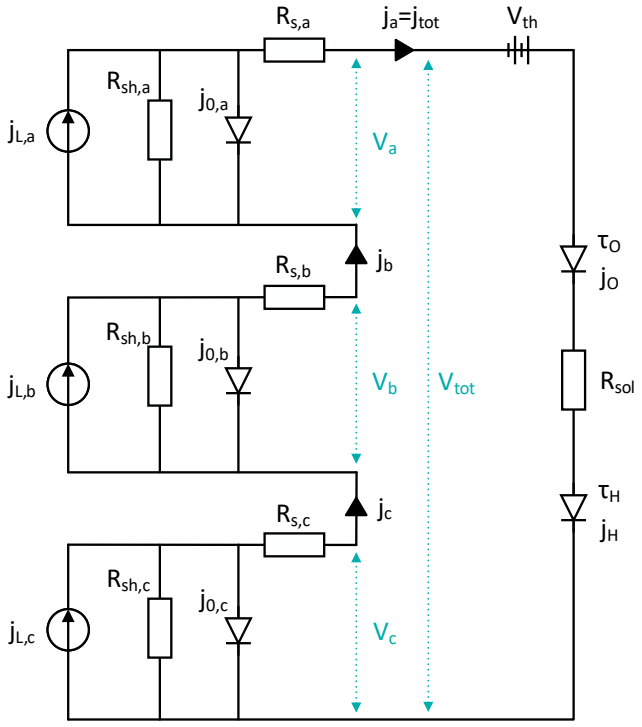

Fig. 3 – Equivalent circuit of a multijunction PV-EC device. In this example, the solar system consists of three different p-n junctions which are made of material a, b and c.

Supplemental Information Section 1). Once the j-V curve is resolved according to the model equations, it is possible to obtain the operating current j_{op} of the system and the associated STH efficiency. Graphically, that means j_{op} is found at the intersection of the solar cell j-V curve and the electrolyzer j-V curve.

In this work, we calibrate and validate the model using experimental data of five different PV-EC cells which are representative of different possible designs and material combinations. These devices and the sources reporting the results are listed in Table 1, together with the light absorber's material, the catalysts used in the cell as well as the reported STH efficiency. Urbain 2015 and Urbain 2016 are both silicon-based devices, the former consists of a solar cell made of a double junction of amorphous silicon (a-Si) while the latter consists of a triple junction made of two layers of amorphous silicon and one layer of micro-crystalline silicon (μc-Si) [16,18]. Jacobsson device includes solar cells connected in series: the photoabsorbers consist of three single-junction copper indium gallium selenide (CIGS) solar cells [17]. Finally, Varadhan and Sun's devices both consist of a double junction solar cell made of an indium gallium phosphide (InGaP) top cell coupled with a gallium arsenide (GaAs) bottom cell [28,29]. Moreover, Sun is the only device that also includes a bipolar membrane, allowing the separation of the O_2 and H_2.

Ideally, separate current-voltage data measurements for each component of the device, i.e. the solar cell and the electrolyzer, are used to calibrate and test the model. However, j-V data are often measured and reported for either some of the components, or for a specific group of components. In such case the data must be inferred by subtracting and adding the available j-V data points based on the equations of the equivalent circuits, which was here necessary for the Varadhan device. Details for the available data can be found in the Supporting Information.

The fitting between model and data is carried out by minimizing the difference between the calculated and measured j-V curve.The objective function f(y) is defined as

$$f(y) = 1 - R^2 = \frac{\sum (y_i - \hat{y}_i)^2}{\sum (y_i - \bar{y})^2} \quad (10)$$

where y_i is the experimental data point i obtained from the j-V curve, $\hat{y}_i$ is the predicted value of y_i by the model and $\bar{y}$ is the mean value of y_i. The objective function is minimized with Matlab (R2018b) optimization routine *fmincon* using the *sequential quadratic programming* (SQP) algorithm. Because of the sensitivity of the Lambert function to changes in the boundary conditions, the model can easily become difficult to solve. While this is not the case for the electrolyzer, whose model is fairly simple, the solar cell can easily show convergence problems. This problem can be tackled by following the approach proposed by Bouzidi et al. [30], where Equation (3) is divided into two equations, one valid for low voltages and one for higher voltages. Therefore, instead of fitting one complex function, the parameters are found by fitting two simpler equations. The overall model is however not changed. More details can be found in the Supporting Information section 2.

In addition to the j-V curve, we compute the solar-to-hydrogen (STH) index, which is a key performance indicator used to compare different solar water splitting devices [31]. It is defined as the ratio between the total chemical energy generated and the total energy input from sunlight illumination:

$$\eta_{STH} = \frac{|j_{op}| E^{\circ} \eta_F}{P_{sun}} \quad (11)$$

where j_{op} is the operating current density, E° (V) is the thermodynamic potential needed to split H_2O in H_2 and O_2 and P_{sun} (mW cm^{-1}) is the incident illumination power density: η_F is the faradaic efficiency; for water splitting, faradaic efficiencies close to 100% are commonly reported in the literature [16], meaning that the photocurrent directly corresponds to the molar hydrogen generation rate and assumes selective and stable catalysts for water splitting.

Fig. 4 reports the parity plots for the solar cells on the left and for the electrolyzer on the right. The parity plots of the solar cells show good agreement with respect to experimental values (R^2 greater than 0.99). For the Sun device, the fitting

Table 1 – List of the 5 PV-EC devices modeled.

Device reference	Light absorber	Catalysts OER/HER	STH
Urbain, 2015, [16]	a-Si/a-Si	RuO_2/Pt	6.8%
Urbain, 2016, [18]	a-Si/a-Si/μc-Si	RuO_2/Ni	8.7%
Jacobsson, [17]	3 CIGS (s)[a]	Pt/Pt	10.5%
Varadhan, [28]	InGaP/GaAs	NiOx/Ni	12.1%
Sun, [29]	InGaP/GaAs	Ni/Ti–CoP	10.0%

[a] (s): solar cells connected in series.

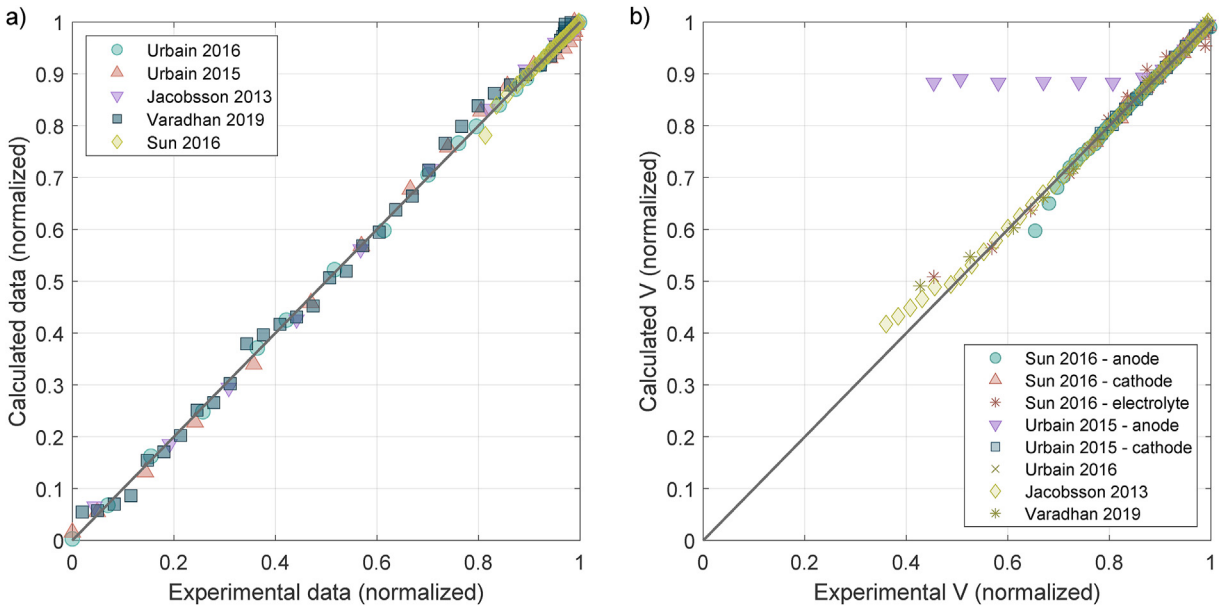

Fig. 4 – Normalized parity plots for a) the solar cell and b) the electrolyzer part. On the x-axis, the experimental data points extracted from literature are displayed, while on the y-axis the output of the model is shown. The data is normalized over the experimental data. A separate Figure for each device is shown in the Supplementary Information.

showed only reliable results for a voltage greater than 1.9 V. This is due to the limited number of experimental data points. Since the j-V curve is nearly horizontal for smaller voltages (see Fig. 5), the resulting fitting is still accurate. The source of error for Varadhan lies in the uncertainty connected to the type of data reported. However, the root mean square error (RMSE) indicates an error of 40 mV in average, which is not significant.

The parity plots of the electrolyzers show more diverse results. In Varadhan et al. [28], different curves were fitted to

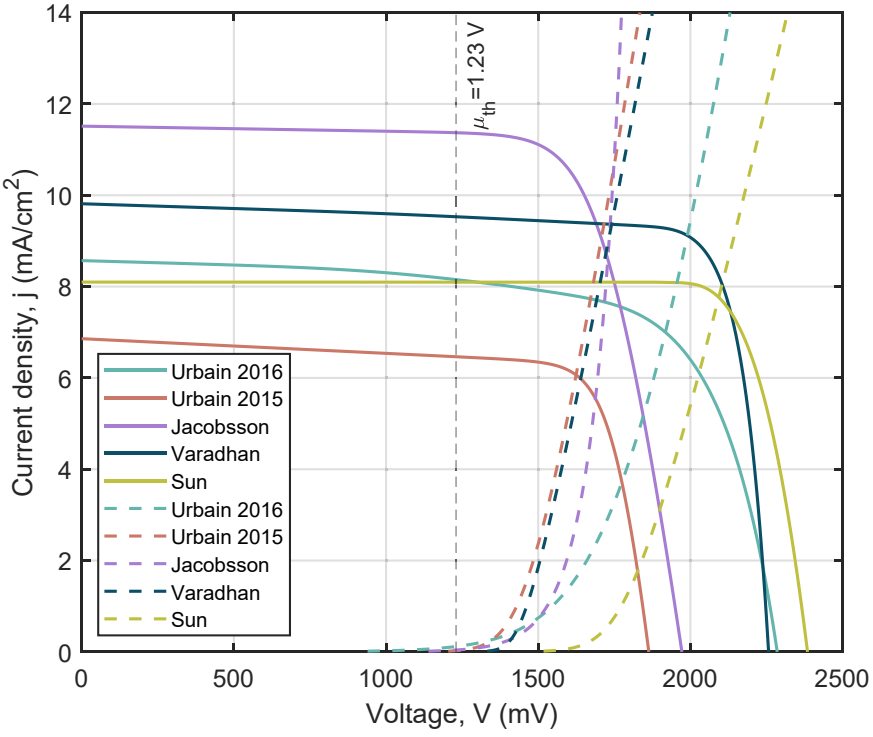

Fig. 5 – j-V curves of the solar cells and electrolyzers of the five PV-EC devices modeled. The j-V characteristics of the devices are measured under P_{sun} = 1 sun illumination (corresponding to 1000 W.m^{-2} or 100 mW.cm^{-2}).

obtain the electrolyzer j-V characteristic. The experimental curve of Urbain 2016 electrolyzer was obtained by subtracting the j-V curve of the whole PV-EC device from the solar cell curve. By doing so, some irregularities appeared at high current densities, probably due to the horizontal part of the two curves, which explains the deviation observed in Fig. 4 b). As for Jacobsson, the electrolyzer j-V curve is available in Ref. [17], but the experimental curve of the electrolyzer is skewed for lower voltages (even below the thermodynamic potential). This anomaly explains the low regression coefficient, which is shown in Figure S3 b). On the other hand, the parity plot shows good results for voltages higher than 1600 mV corresponding to a current density of around 2 mA cm^{-2}, and since the device is mainly operating for current densities around 5 mA cm^{-2} low voltage area should simply be disregarded. The electrolyzer curve of Varadhan depicts the overpotential of the anode combined with the voltage drop due to the solution resistance, and the model describes accurately the system. Urbain 2015 reports a value of R_{sol} which was measured by impedance spectroscopy. The data available for Urbain 2015 is very detailed since the j-V curves of all the components of the electrolyzer are published. Also in this case the model shows good agreement with experimental data (highest RMSE is obtained for the cathod and limited to 6 mV). As for Sun, experimental data for anode, cathode, and electrolyte were available, allowing for a detail tuning of the model.

The values of the fitting parameters of each junction of the solar cells are compiled in Table 2. The values of the photogenerated current densities j_L are in line with the experimental short current densities. In the Jacobsson cell, the photogenerated current displayed is approximately three times higher than the rest of the devices due to the fact that the light absorbers consist of three solar cells connected in series. As for the other devices, the standard construction is a tandem device, where cells are also connected in series, but the whole surface area belongs to the same cell. In the Jacobsson device the cells are connected in series instead of being stacked on top of each other, thus the available light collector area is three times higher. The photogenerated current of the whole device is therefore $j_L/3 \approx 11.5$ mA cm^{-2}, according to Equation (5). CIGS solar cells produce a high current density but suffer from low voltage.

The saturation current densities j_0 range from 10^{-4} to 10^{-16}, showing no clear connection with the respective material. j_0 depends on many factors, among which the type and number of junction [32]. In particular, Urbain 2015 and Sun devices exhibit very low saturation current densities while, on the contrary, the j_0 values of Urbain 2016 device are rather high. The calculated saturation current densities appear to be in range with the values reported in the literature. For example, the modeling results by Winkler et al. reveal value of $j_0 = 4\ 10^{-10}$ mA cm^{-2} [26].

The calculated series resistance R_s for four out of the five PV-EC devives range from 0.5 to 5 Ω cm^2, in line with the few values reported in the literature [26,30]. Urbain 2016 device shows particularly low values of R_s, which may be explained by a trade-off between j_0 and R_s since both parameters influence the open-circuit voltage, also justifying the high calculated values of j_0 compared to the other devices.

The values obtained for the shunt resistances R_{sh} are satisfactory since the expected range is around 10^3 to 10^6 [33].

Finally, the ideality factor n_i varies typically between 1 and 2 depending on whether the recombination losses occur in the space-charge region ($n_i \approx 1$) or in the depletion region ($n_i \approx 2$) [34,35]. Yet, ideality factors greater than 2 can sometimes be observed in heterojunction solar cells [36], such as in Urbain 2016 or Sun devices.

The values obtained for the electrolyzer part of the devices are compiled in Table 3. The parameters are in line with values provided in literature [26]. Since the experimental data of the cathode of the Varadhan cell was not available (see Supporting Information 3), for this device the losses of the cathode were not considered. For all devices, the exchange current density at the anode j_O^0 is lower than the exchange current density at the cathode j_H^0, which can be explained by the lower

Table 3 – Electrolyzer parameters found after fitting the experimental j-V curves of the 5 PV-EC devices. τ_O and τ_H are expressed in millivolt per decade. R_{sol} of Sun device was directly provided in the literature.

	τ_O	τ_H	j_O^0	j_H^0	R_{sol}
	mV/dec	mV/dec	mA.cm^{-2}	mA.cm^{-2}	Ω.cm^2
Urbain 2015	57	54	1.7×10^{-3}	0.45	21.3
Urbain 2016	154	169	0.11	0.13	16
Jacobsson	177	36	0.04	0.26	22
Varadhan	57	–	2×10^{-4}	–	27
Sun	51	72	1×10^{-9}	0.15	31

Table 2 – Solar cell parameters of each junction calculated by fitting the equations of the equivalent circuit to the experimental j-V curves of the 5 PV-EC devices. The light absorber material used in each junction is also being reminded.

	Material	j_L	j_0	R_s	R_{sh}	n_i
		mA.cm^{-2}	mA.cm^{-2}	Ω.cm^2	Ω.cm^2	
Urbain et al. 2015	a-Si	5.2	2×10^{-14}	5.2	1551	1.1
Urbain et al. 2016	a-Si	6.80	9.8×10^{-9}	0.36	3317	1.0
	μc-Si	6.84	2.25×10^{-8}	1.50	1481	1.6
Jacobsson et al.	CIGS	34.6	3×10^{-10}	1.7	1001	1.0
Varadhan et al.	InGaP	9.7	1×10^{-9}	0.5	2779	1.1
	GaAs	10.0	3×10^{-9}	0.6	2030	1.8
Sun et al.	InGaP	8.1	1×10^{-16}	3.6	8.80×10^5	1.2
	GaAs	9.1	3×10^{-7}	3.6	1.01×10^4	2.7

kinetics of the OER. The solution resistance varies between 16 and 31 Ω cm^2, which is in line with the range provided by Winkler et al. (0–60 Ω cm^2). The resistance of Sun device is slightly higher, presumably due to the membrane between the electrodes that slows down the circulation of the protons. The solution resistance also depends on the distance between the two electrodes; the distance is usually around 2 cm. But this information is not always provided.

The resulting j-V curves for the solar cell and the electrolyzer are shown in Fig. 5. When comparing the different devices, we can link the photoabsorber and electrolyzer curve to the characteristics of the device in terms of materials and design. For instance, the two devices comprising platinum electrodes, Urbain 2015 and Jacobsson, exhibit very low overpotentials at the electrolyzer even at high current density. Platinum is a very efficient, yet expensive catalyst used to demonstrate proofs of concept [17]. Similarly, the figure shows that CIGS solar cells used in Jacobsson device provide a high current density but suffer from low voltages. Therefore, coupling the CIGS solar cells with the catalysts used in Sun device for example (nickel and cobalt phosphide) would yield a much lower efficiency. Sun device succeeds to exhibit a high efficiency because of the InGaP/GaAs junction that provides a sufficient voltage.

It is worth stressing that PV-EC models based on equivalent electric circuit build upon interpretation of the device physical behaviour but are largely empirical. Therefore the physical interpretation of the model parameters must be taken with caution. Yet, the main scope of such simple model is to reproduce mathematically the j-V characteristics as accurately as possible, which is found to be overall satisfying.

Finally, we can compare the model findings with the experimental value of the sun to hydrogen efficiency. The results are reported in Table 4. Overall, we notice that the agreement between experiments and model is good. The largest difference is observed for Urbain 2015 and is mainly due to the error in extracting the experimental data from the graph in the paper. More specifically, while we obtain a R^2 larger than 0.999, we find a $R_{sol} = 23.5\ \Omega\ cm^2$ compared to $R_{sol} = 21.3\ \Omega\ cm^2$ provided in the paper; this is due to the small discreptancy between the data used to fit the model and those obtained experimentally. For Varadhan and Sun, the difference is probably due to the lack of the component-specific data points. On the other hand, the calculated efficiency of Urbain 2016 and Jacobsson is almost equal to the reported efficiency, while the others are reasonably close for such simple model.

In summary, the model shows good agreement with experimental values, however, data availability and quality are key for tuning the model accurately.

PV-EC model for varying illumination and tilt angle

The model presented before was fitted using experimental data measured under artificial sunlight at standard condition, AM 1.5G and an illumination of 100 mW cm^{-2} equal to 1 sun. However, PV-EC devices will hardly work under these conditions, and to reflect more realistic performance and predict the yearly average STH efficiency, we need to include the effect of illumination as well as the influence of different tilt angles.

Solar illumination directly influences the photogenerated current j_L proportionally [37]:

$$j_L = \frac{\hat{j}_L P_{sun}}{\hat{P}_{sun}} \tag{12}$$

where $\hat{j}_L$ is the nominal photogenerated current as calculated under $\hat{P}_{sun} = 1$ sun illumination and P_{sun} the real illumination. As shown in Fig. 6 for Urbain 2016, a new operating point (j_{op}) on the j-V plane is established for every value of j_L. In real application, j_{op} becomes a time-dependent value. As a result, the matching between photoabsorber and electrolyzer needs to be resolved at any time instant (i.e. for different irradiation values). When comparing all devices considered in this work for different irradiation values (see Fig. 7 a) we note that, while Varadhan's device achieves highest j_{op} and STH efficiency at 1 sun, Jacobsson's device is the most performing for $P_{sun} < 0.7$ sun. This stems from the current density of the PV cell, which is higher compared to the other devices. On the other hand, Sun's device shows the most stable performance, since its STH efficiency remains almost constant over the whole illumination range. The high efficiency is due to the InGaP/GaAs tandem-junction, which provides a sufficiently high voltage to drive the water-splitting reaction. The efficiency curves of Urbain 2015 and Urbain 2016 show the same trend as the Varadhan device: the higher the illumination the higher the STH. In order to understand on an yearly base what device is the most performing, a time-discretized analysis is required.

Comparison of PV-EC cells under varying working conditions

In this section, we compare the different devices with regards to their yearly performance under varying time- and space-

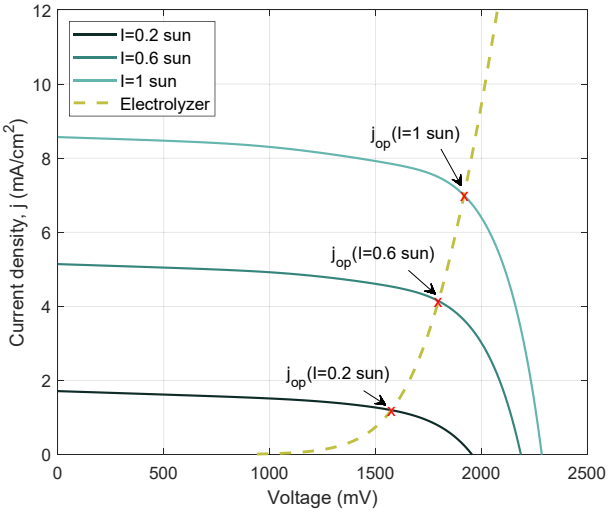

Fig. 6 – The effect of different illumination intensities for Urbain 2016 device as an example. The red x shows the operating point j_{op} of the solar cell and the electrolyzer. (For interpretation of the references to color in this figure legend, the reader is referred to the Web version of this article.)

Table 4 – Calculated STH efficiencies based on the fitted devices.

	Calculated STH	Reported STH
Urbain 2015	7.5%	6.8%
Urbain 2016	8.6%	8.7%
Jacobsson	10.6%	10.5%
Varadhan	11.6%	12.1%
Sun	9.6%	10.0%

dependant illumination, and tilt angle. While we do not directly compute H_2 costs, which are highly uncertain and out of the scope here, we compare the devices using the specific area a (in m^2/t_{H_2}), i.e. the cell area needed to produce one ton of H_2 per year. This is a proxy for the system cost and it embeds the thermodynamic performance of the device throughout the year. The cell area a can be derived from the amount of energy stored as hydrogen molecules over the year per square meter of photoabsorber collector area, $e_{H_2}^{year}$ (kJ/(m^2 year)), according to Equation (13):

$$a_{H_2}^{year} = \frac{\Delta\overline{G}_{H_2}^{0}}{e_{H_2}^{year}} \tag{13}$$

where $\Delta\overline{G}_{H_2}^{0}$ the Gibbs free energy of the water splitting reaction ($\Delta\overline{G}_{H_2}^{0} = 118.6$ MJ/kg). Notably, $e_{H_2}^{year}$ depends on the solar energy input P_{sun} and on the STH efficiency η_{STH} of the device, where both P_{sun} and η_{STH} are time dependent. We can therefore write:

$$e_{H_2}^{year} = \int_{t_0}^{t_{end}} \eta_{STH}(t) P_{sun}(t) dt \tag{14}$$

Plugging in η_{STH} from Equation (11) in the expression above, and noting that we can include the time dependency via hourly-averaged values of j_{op} in combination with hourly data of solar irradiance (thus substituting the integral with an hourly-resolved sum over the hours of the year), Equation (14) can be rewritten as:

$$e_{H_2}^{year} = \sum_{i=1}^{i=8760} \bar{j}_{op,\,i} E^{\circ} \eta_F \tag{15}$$

where $e_{H_2}^{year}$ is here provided in (kWh). This expression, in combination with irradiance-dependent modelling of the PV-EC cell, allows for calculating the performance of the cell with real-world, space-defined, data and tilt angle. Note that the tilt angle, which for PV applications is typically a design variable that can be freely optimized, it is here bounded by the fluid dynamic within the PV-EC cell: while vertical modules allow for a straightforward gas/liquid dynamic they are penalized from a tilt angle perspective. The contrary holds for horizontal panels. In this work, we consider two different locations as possible PV-EC sites: Sevilla in Spain (with high illumination), and Utrecht in the Netherlands (with lower illumination). The solar irradiance data, more precisely the global horizontal irradiance, in Sevilla and in Utrecht was obtained from Solcast with an hourly resolution for 2019 [38]. Starting from these data, the effect of the tilt angles (in the range of 0–90°) was included applying the System Advisor Model (SAM) from the National Renewable Energy Laboratory (NREL) [39]. The azimuth angle was instead kept constant at 180°as well as the temperature of the system. The performance of catalysts and electrolytes were considered independent of the illumination, i.e. no electrodes degradation as function of sunlight were considered [40].

Fig. 8 shows the daily average η_{STH} for hours with irradiance larger than 0 over the full year. This figure was obtained with Urbain 2016 as exemplary device, which can reach an efficiency in the range of η_{STH} = 5.9–8.6% (Fig. 7). Moreover, three different curves for three different tilt angles are shown (0, 45, and 90°). The yearly trend is as expected for any photovoltaic device: the maximum production is reached in summer and the minimum in winter. However, the height of the maximum in summer and the extent of the valley in winter depends on the tilt angle: while low tilt angles favor the maximum STH efficiency in summer, a vertical device has

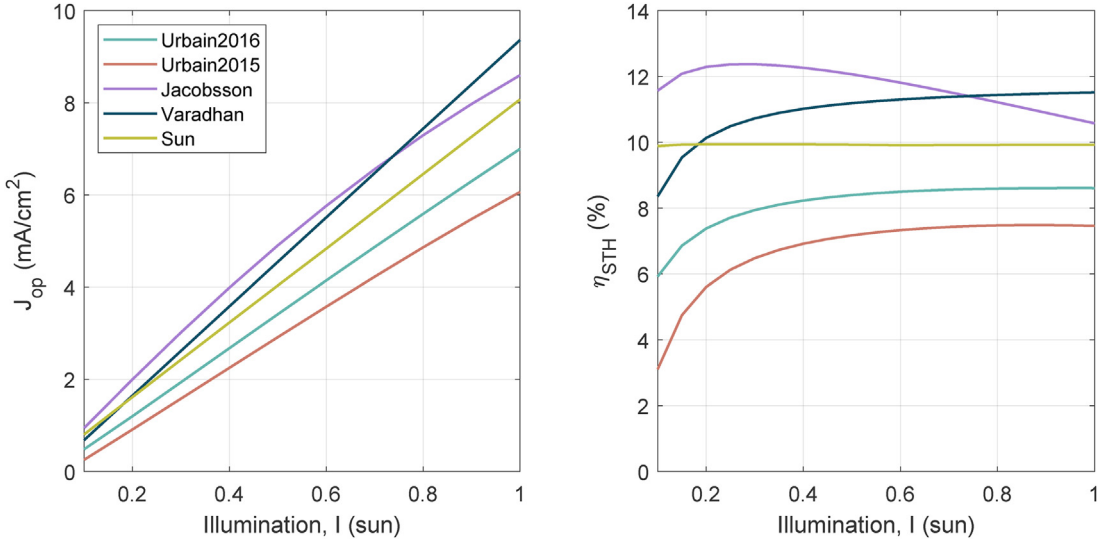

Fig. 7 – The effect of different illumination intensities on a) the operating point j_{op} between the PV cell and the electrolyzer, and b) the STH efficiency of the five PV-EC devices.

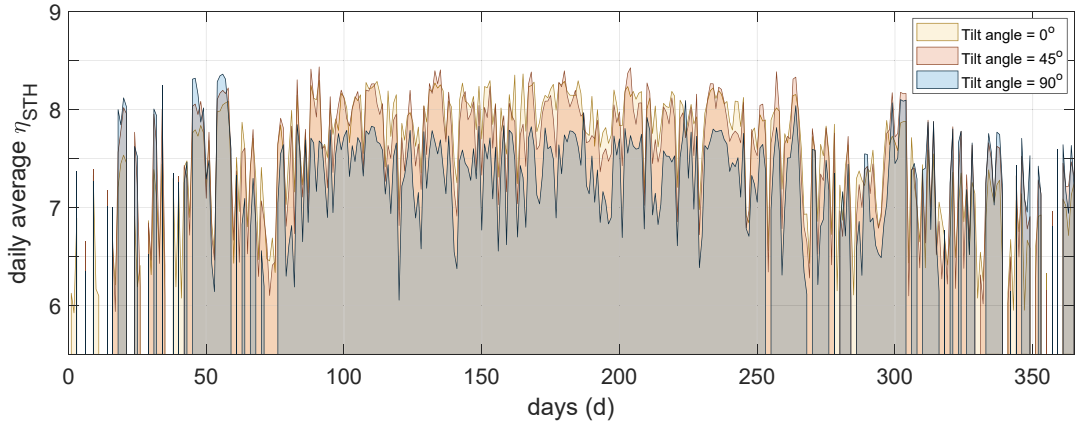

Fig. 8 – Average daily STH efficiency over the year for Utrecht using the Urbain 2016 device at different tilt angles (yellow for 0°, red for 45°, and blue for 90°). (For interpretation of the references to color in this figure legend, the reader is referred to the Web version of this article.)

overall a more constant production through the year. Notably, only a minor difference exists between tilt angles in the range 0–45°. However, it is worth stressing that tilt angles between 0 and 15°would be challenging from a practical point of view, as the produced gases would tend to diffuse through the device rather than being collecting because of natural buoyancy. On the other hand, increasing the tilt angle is overall conducive to a lower average STH efficiency throughout the year, although it has a minor impact: for a tilt angle of 60°, the average STH efficiency decreases of about 0.5% compared to a horizontal panel. Finally, it can be noted that the daily STH efficiency is often lower then the STH efficiency measured under one sun constant illumination.

It is important to stress that we do consider the working hours for the calculation of the average η_{STH}. Therefore, effects of shading are not included in our analysis. These effects are dependent on the specific design of the cell, especially on the EC part, and can be an important source of decrease. However, adapting our model to include this effect is out of scope of the present study.

The specific area a for H_2 production brings eventually together all dependencies in one parameter. Fig. 9 shows a for the different devices considered here, at varying tilt angle and location (Utrecht on the left and Sevilla on the right). Moreover, we benchmark the 5 PV-EC devices with the standalone PV panel + electrolyzer configuration (PV-E), which was calculated using data published by Clarke et al. [41]. The minimum specific area a is found at an angle of around 40°, which can be directly correlated to the profile of the irradiation intensity (maximum at also around 40°). When changing the azimuth angle, the optimum changes slightly. It can be noted that the area requirement for the PV-EC cell is always larger than the PV-E system. However, Jacobsson and Varadhan devices perform close to the reference system; they therefore show rather clearly the preferred direction of PV-EC development (as far as costs are excluded).

When comparing the two locations, and since the total energy input in Utrecht (3.8 GJ/m^2) is roughly half of that in Sevilla (6.8 GJ/m^2) during the same year, a is in general clearly higher in Utrecht. The associated operating hours amount to

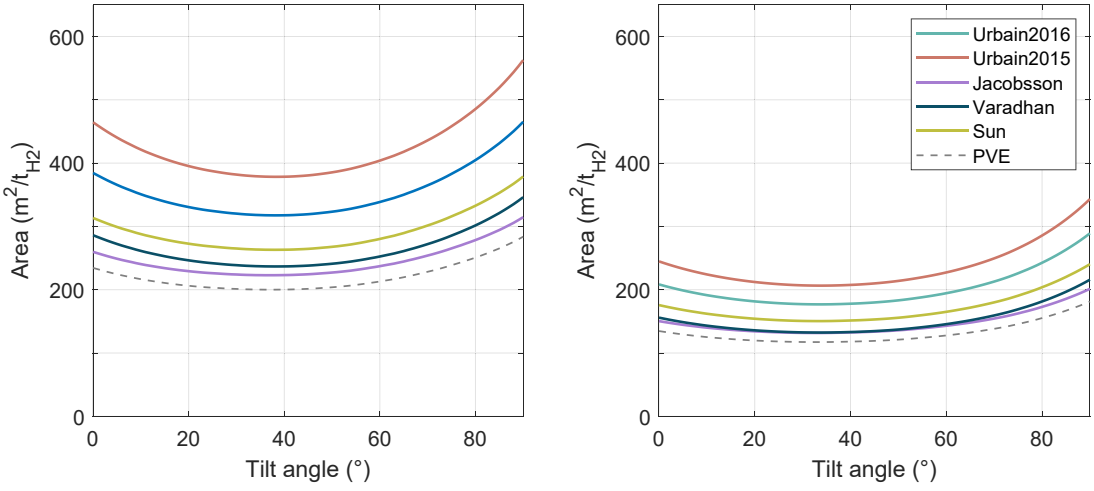

Fig. 9 – Specific area a for the 5 PV-EC devices and a PV-E device dependent on the tilt angle (tilt = 0–90°). a) Utrecht. b) Sevilla. The azimuth angle is fixed at 180°.

3767 h in Sevilla and 3034 h in Utrecht. The distribution of the STH efficiency in Utrecht and Sevilla for the whole year can be found in the Supplemental Information in Figure S5.

For both locations, the rank order of the PV-EC devices is the same, with Urbain 2015 requiring the largest surface area and Jacobsson the smallest. The ranking is a result of the dependency of the STH efficiency on the illumination intensity shown in Fig. 7 b. Having the highest efficiency, the PV-E device shows the best performance.

A summary of the effect of location and its comparison with the ideal one-sun conditions is shown in Table 5 for a fixed tilt angle of 60°. While the Varadhan device has the highest efficiency under one-sun illumination, the Jacobsson device reaches a higher average efficiency, especially for Utrecht. This is because the Jacobsson cell shows its best performance for an illumination intensity of around 0.2 sun (7 b) and the average illumination in Sevilla is 0.50 sun, compared to 0.35 sun in Utrecht (in 2019, but generally valid). Therefore, the Jacobsson system is relatively more efficient in Utrecht than in Sevilla, whereas the Varadhan device performs well under high illumination, and has poor performance in Utrecht. On the other hand, the average STH efficiency of the Jacobsson and Varadhan device are similar in Sevilla, resulting in a similar specific area (Fig. 9). This analysis shows that different PV-EC devices might be optimal for different locations irrespective of their efficiency under one-sun conditions, and that real operating conditions (time- and space-dependent) are required to fairly compare devices. Overall, PV-EC development should target real world varying conditions: High STH efficiency under ideal illumination does not fully reveal the cell performance.

At the same time, it is worth stressing that the model presented here provides only a first approximation of the behaviour of the system under real-world conditions. In addition to varying irradiation, the ambient temperature should be included as it has a significant impact on the performance of PV-EC devices (it influences both the solar cell, increasing the thermal voltage V_{th}), and the electrolyser, whose potential decreases significantly with the temperature [40]). Moreover, aging and performance decay should also be included for a full evaluation. These effects will however further exacerbate the dependency of the device on the ambient conditions, making the evaluation under non-ideal conditions even more necessary.

Table 5 – Specific area *a* and average STH efficiency based on the solar irradiance data of 2019 in Utrecht, Netherlands, and in Sevilla, Spain with a tilt angle of 60°. The STH efficiency under 1 sun is also reported for comparison purposes. For very low illumination intensities inferior to 0.1 sun, the model assumes no output. The PV-E device was calculated using data from Ref. [41].

	Utrecht		Sevilla		η_{STH}
	Area	Average η_{STH}	Area	Average η_{STH}	1 sun
	m^2/t_{H2}	%	m^2/t_{H2}	%	%
Urbain 2015	544	5.79	227	7.18	7.5
Urbain 2016	450	7.50	195	8.40	8.6
Jacobsson	309	12.33	143	11.43	10.6
Varadhan	335	10.26	146	11.24	11.6
Sun	367	9.94	165	9.93	9.93
PV-E	213	13.28	135	12.81	12.1

Conclusion

In this work we presented a simple, yet insightful, framework to model photo-electrochemical water splitting devices using an equivalent circuits approach. In the first part of the paper, we derived the model equations, described the resolution strategy and validated the model with existing experimental data for ideal one-sun conditions. To this end, current density-voltage data for five different devices were used, where the devices were selected depending on the quality and type of experimental data available. The model showed good agreement with the experimental results. Within the limits of the model, we also tried to provide a physical explanation of the different performance as function of the cell materials and design.

To extend the model to real operating conditions, we presented a simple modification of the model that takes into account real irradiation data. The five devices were therefore compared at varying irradiation: Three of the five devices showed an optimal STH efficiency for ideal illumination, one showed rather constant STH efficiency, while one showed an optimal efficiency for low irradiation, i.e. 0.25 sun. Moreover, the most performing device varies depending on the irradiation.

In the second part of the paper we used the developed irradiation-dependent model to evaluate the yearly performance of the considered cells at different tilt angles and different locations, i.e. (i) Sevilla in Spain and (ii) Utrecht in the Netherlands. The cells were therefore compared using the specific area needed to produce 1 ton of hydrogen per year. We were able to identify the cell type with lower specific area; moreover we found that irrespective of the cell a tilt angle in the range of 25-45° is optimal for Utrecht and Sevilla.

Overall, the presented model is a powerfull tool for untangling PV-EC performance and comparing different concepts. The availability of high quality experimental data remains however a key requirement for the use of this model.

Declaration of competing interest

The authors declare that they have no known competing financial interests or personal relationships that could have appeared to influence the work reported in this paper.

Acknowledgements

Alexa Grimm is financially supported by Shell Global Solutions.

Appendix A. Supplementary data

Supplementary data to this article can be found online at https://doi.org/10.1016/j.ijhydene.2022.01.223.

REFERENCES

[1] IEA. The future of hydrogen. Paris: IEA; 2019. URL, https://www.iea.org/reports/the-future-of-hydrogen. 2019.

[2] Fujishima A, Honda K. Electrochemical photolysis of water at a semiconductor electrode. nature 1972;238(5358):37–8.

[3] Rabell GO, Cruz MA, Juárez-Ramírez I. Photoelectrochemical (PEC) analysis of ZnO/Al photoelectrodes and its photocatalytic activity for hydrogen production. Int J Hydrogen Energy 2022.

[4] Braiek Z, Ben Naceur J, Jrad F, Ben Assaker I, Chtourou R. Novel synthesis of graphene oxide/In2S3/TiO2 NRs heterojunction photoanode for enhanced photoelectrochemical (PEC) performance. Int J Hydrogen Energy 2022;47(6):3655–66. https://doi.org/10.1016/J.IJHYDENE.2021.10.268. ISSN 0360-3199.

[5] Bai S, Han J, Zhang K, Zhao Y, Luo R, Li D, Chen A. rGO decorated semiconductor heterojunction of BiVO4/NiO to enhance PEC water splitting efficiency. ISSN 0360-3199 Int J Hydrogen Energy 2022;47(7):4375–85. https://doi.org/10.1016/J.IJHYDENE.2021.11.122. URL, https://linkinghub.elsevier.com/retrieve/pii/S0360319921045092.

[6] Turan B, Becker JP, Urbain F, Finger F, Rau U, Haas S. Upscaling of integrated photoelectrochemical water-splitting devices to large areas. Nat Commun 2016;7(1):1–9. https://doi.org/10.1038/ncomms12681. ISSN 20411723.

[7] Nielander AC, Shaner MR, Papadantonakis KM, Francis SA, Lewis NS. A taxonomy for solar fuels generators. ISSN 17545706 Energy Environ Sci 2015;8(1):16–25. https://doi.org/10.1039/c4ee02251c. URL, https://pubs.rsc.org/en/content/articlehtml/2015/ee/c4ee02251c https://pubs.rsc.org/en/content/articlelanding/2015/ee/c4ee02251c.

[8] Jacobsson TJ, Fjällström V, Edoff M, Edvinsson T. Sustainable solar hydrogen production: from photoelectrochemical cells to PV-electrolyzers and back again. ISSN 17545706 Energy Environ Sci 2014;7(7):2056–70. https://doi.org/10.1039/c4ee00754a. URL, https://pubs.rsc.org/en/content/articlehtml/2014/ee/c4ee00754a.

[9] Hamdani IR, Bhaskarwar AN. Recent progress in material selection and device designs for photoelectrochemical water-splitting. Renew Sustain Energy Rev 2021;138:110503. https://doi.org/10.1016/J.RSER.2020.110503. ISSN 1364-0321.

[10] Wang Q, Hisatomi T, Jia Q, Tokudome H, Zhong M, Wang C, Pan Z, Takata T, Nakabayashi M, Shibata N, Li Y, Sharp ID, Kudo A, Yamada T, Domen K. Scalable water splitting on particulate photocatalyst sheets with a solar-to-hydrogen energy conversion efficiency exceeding 1%. URL, www.nature.com/naturematerials.

[11] Maeda K, Takata T, Hara M, Saito N, Inoue Y, Kobayashi H, Domen K. GaN:ZnO solid solution as a photocatalyst for visible-light-driven overall water splitting. URL, https://pubs.acs.org/sharingguidelines.

[12] Jia J, Seitz LC, Benck JD, Huo Y, Chen Y, Ng JWD, Bilir T, Harris JS, Jaramillo TF. Solar water splitting by photovoltaic-electrolysis with a solar-to-hydrogen efficiency over 30%. ISSN 20411723 Nat Commun 2016;7(May):1–6. https://doi.org/10.1038/ncomms13237.

[13] Kim JH, Hansora D, Sharma P, Jang JW, Lee JS. Toward practical solar hydrogen production-an artificial photosynthetic leaf-to-farm challenge. Chem Soc Rev 2019;48(7):1908–71. https://doi.org/10.1039/c8cs00699g. ISSN 14604744.

[14] Rongé J, Bosserez T, Martel D, Nervi C, Boarino L, Taulelle F, Decher G, Bordiga S, Martens JA. Monolithic cells for solar fuels. URL, www.rsc.org/chemsocrev; 2014.

[15] Reece SY, Hamel JA, Sung K, Jarvi TD, Esswein AJ, Pijpers JJ, Nocera DG. Wireless solar water splitting using silicon-based semiconductors and earth-abundant catalysts. Tech Rep 2011;6056. https://doi.org/10.1126/science.1209816.

[16] Urbain F, Smirnov V, Becker JP, Rau U, Ziegler J, Kaiser B, Jaegermann W, Finger F. Application and modeling of an integrated amorphous silicon tandem based device for solar water splitting. ISSN 09270248 Sol Energy Mater Sol Cell 2015;140:275–80. https://doi.org/10.1016/j.solmat.2015.04.013.

[17] Jacobsson TJ, Fjällström V, Sahlberg M, Edoff M, Edvinsson T. A monolithic device for solar water splitting based on series interconnected thin film absorbers reaching over 10% solar-to-hydrogen efficiency. ISSN 1754-5692 Energy Environ Sci 2013;6(12):3676. https://doi.org/10.1039/c3ee42519c. URL, http://xlink.rsc.org/?DOI=c3ee42519c.

[18] Urbain F, Smirnov V, Becker JP, Lambertz A, Yang F, Ziegler J, Kaiser B, Jaegermann W, Rau U, Finger F. Multijunction Si photocathodes with tunable photovoltages from 2.0 v to 2.8 v for light induced water splitting. ISSN 17545706 Energy Environ Sci 2016;9(1):145–54. https://doi.org/10.1039/c5ee02393a. URL, https://pubs-rsc-org.proxy.library.uu.nl/en/content/articlelanding/2016/ee/c5ee02393a#!divAbstract.

[19] Cheng WH, Richter MH, May MM, Ohlmann J, Lackner D, Dimroth F, Hannappel T, Atwater HA, Lewerenz HJ. Monolithic photoelectrochemical device for direct water splitting with 19% efficiency. ACS Energy Lett 2018;3(8):1795–800. https://doi.org/10.1021/acsenergylett.8b00920. ISSN 23808195.

[20] Han L, Abdi FF, Van De Krol R, Liu R, Huang Z, Lewerenz HJ, Dam B, Zeman M, Smets AH. Efficient water-splitting device based on a bismuth vanadate photoanode and thin-film silicon solar cells. ISSN 1864564X ChemSusChem 2014;7(10):2832–8. https://doi.org/10.1002/cssc.201402456. URL, https://chemistry-europe-onlinelibrary-wiley-com.proxy.library.uu.nl/doi/full/10.1002/cssc.201402456 https://chemistry-europe-onlinelibrary-wiley-com.proxy.library.uu.nl/doi/abs/10.1002/cssc.201402456.

[21] Kobayashi H, Sato N, Orita M, Kuang Y, Kaneko H, Minegishi T, Yamada T, Domen K. Development of highly efficient CuIn0.5Ga0.5Se2-based photocathode and application to overall solar driven water splitting. Energy Environ Sci 2018;11(10):3003–9. https://doi.org/10.1039/c8ee01783b. ISSN 17545706.

[22] Sharifi T, Larsen C, Wang J, Kwong WL, Gracia-Espino E, Mercier G, Messinger J, Wågberg T, Edman L. Toward a low-cost artificial leaf: driving carbon-based and bifunctional catalyst electrodes with solution-processed perovskite photovoltaics. Adv Energy Mater 2016;6(20):1–10. https://doi.org/10.1002/aenm.201600738. ISSN 16146840.

[23] Nguyen PD, Duong TM, Tran PD. Current progress and challenges in engineering viable artificial leaf for solar water splitting. ISSN 24682179 J Sci: Adv Mater Dev 2017;2(4):399–417. https://doi.org/10.1016/j.jsamd.2017.08.006.

[24] Ager JW, Shaner MR, Walczak KA, Sharp ID, Ardo S. Experimental demonstrations of spontaneous, solar-driven photoelectrochemical water splitting. ISSN 17545706 Energy Environ Sci 2015;8(10):2811–24. https://doi.org/10.1039/c5ee00457h.

[25] Alfaifi BY, Ullah H, Alfaifi S, Tahir AA, Mallick TK. Photoelectrochemical solar water splitting: from basic

principles to advanced devices. Veruscript Funct Nanomater 2018;2(February). https://doi.org/10.22261/fnan.bdjoc3. BDJOC3.
[26] Winkler MT, Cox CR, Nocera DG, Buonassisi T. Modeling integrated photovoltaic–electrochemical devices using steady-state equivalent circuits. Proc Natl Acad Sci 2013;110(12):E1076–82.
[27] Fathabadi H. Lambert W function-based technique for tracking the maximum power point of PV modules connected in various configurations. Renew Energy 2015;74:214–26. https://doi.org/10.1016/j.renene.2014.07.059. ISSN 09601481.
[28] Varadhan P, Fu HC, Kao YC, Horng RH, He JH. An efficient and stable photoelectrochemical system with 9% solar-to-hydrogen conversion efficiency via InGaP/GaAs double junction. Nat Commun 2019;10(1):1–9. https://doi.org/10.1038/s41467-019-12977-x. ISSN 20411723.
[29] Sun K, Liu R, Chen Y, Verlage E, Lewis NS, Xiang C. A stabilized, intrinsically safe, 10% efficient, solar-driven water-splitting cell incorporating earth-abundant electrocatalysts with steady-state pH gradients and product separation enabled by a bipolar membrane. ISSN 16146840 Adv Energy Mater 2016;6(13):1600379. https://doi.org/10.1002/aenm.201600379.
[30] Bouzidi K, Chegaar M, Bouhemadou A. Solar cells parameters evaluation considering the series and shunt resistance. Sol Energy Mater Sol Cell 2007;91(18):1647–51. https://doi.org/10.1016/j.solmat.2007.05.019. ISSN 09270248.
[31] Döscher H, Geisz JF, Deutsch TG, Turner JA. Sunlight absorption in water–efficiency and design implications for photoelectrochemical devices. Energy Environ Sci 2014;7(9):2951–6.
[32] Neville RC. Solar cell configuration and performance. In: Solar energy conversion: the solar cell. 2nd ed. Elsevier B.V.; 1995. p. 197–256. https://doi.org/10.1016/B978-044489818-0/50006-5. chap. CHAPTER VI.
[33] Somasundaran P, Gupta R. Evaluation of shunt losses in industrial silicon solar cells. Int J Photoenergy 2016;2016.
[34] Usami A. Optical and electrical modeling of nanocrystalline solar cells. In: Nanostructured materials for solar energy conversion; 2006. https://doi.org/10.1016/B978-044452844-5/50004-4. ISBN 9780444528445.
[35] Honsberg C, Bowden S. PVEducation. URL, https://www.pveducation.org/; 2019.
[36] Chavali RVK, Wilcox JR, Ray B, Gray JL, Alam MA. Correlated nonideal effects of dark and light I–V characteristics in a-Si/c-Si heterojunction solar cells. ISSN 2156-3381 IEEE J Photovolt 2014;4(3):763–71. https://doi.org/10.1109/JPHOTOV.2014.2307171. URL, http://ieeexplore.ieee.org/document/6777567/.
[37] Sayedin F, Maroufmashat A, Sattari S, Elkamel A, Fowler M. Optimization of photovoltaic electrolyzer hybrid systems; taking into account the effect of climate conditions. Energy Convers Manag 2016;118:438–49.
[38] Solcast. Solar forecasting & solar irradiance data. 2020. https://solcast.com/.
[39] National Renewable Energy Laboratory. System Advisor model (SAM), golden, CO (United States). 2020. p. 11–8. version 2020.2.29 (SAM 2020.2.29).
[40] Dias P, Lopes T, Andrade L, Mendes A. Temperature effect on water splitting using a Si-doped hematite photoanode. ISSN 03787753 J Power Sources 2014;272:567–80. https://doi.org/10.1016/j.jpowsour.2014.08.108.
[41] Clarke R, Giddey S, Ciacchi FT, Badwal SP, Paul B, Andrews J. Direct coupling of an electrolyser to a solar PV system for generating hydrogen. ISSN 03603199 Int J Hydrogen Energy 2009;34(6):2531–42. https://doi.org/10.1016/j.ijhydene.2009.01.053. URL, http://linkinghub.elsevier.com/retrieve/pii/S0360319909001244.